Evaluation of rare earth on Layered Silicates under Subcritical Conditions: Effect of the Framework and Interlayer Space Composition

Pablo Chain[1], Agustín Cota[1,2], Said El Mrabet[1], Esperanza Pavón[3], M. Carolina Pazos[1], María D. Alba[1*]

[1]Instituto Ciencia de los Materiales de Sevilla- Departamento de Química Inorgánica, CSIC-Universidad de Sevilla. Avda. Américo Vespucio, 49. 41092-Sevilla (Spain)

[2]Laboratorio de Rayos-X. Centro de Investigación, Tecnología e Investigación de la Universidad de Sevilla (CITIUS). Avda. Reina Mercedes, 4b. 41012-Sevilla (Spain)

[3]Unité de Catalyse et de Chimie du Solide, UCCS, CNRS, UMR8181, Université Lille Nord de France, 59655 Villeneuve d'Ascq (FRANCE)

Abstract

Clay-based minerals are considered to be an important component in backfill barriers due to both their ability to seal and adsorb radioactive waste and to interact chemically with it under subcritical conditions. Herein, we describe a systematic study of the properties of layered silicates that could affect their hydrothermal reactivity, namely type of layers, octahedral occupancy, origin and total amount of the layer charge, and nature of the interlayer cation. The silicates studied were selected on the basis of their different characteristics associated with these properties and were treated hydrothermally at 300ºC for 48 h in a $7.3 \cdot 10^{-2}$ M $Lu(NO_3)_3 \cdot 3.6H_2O$ solution. The final products were analyzed by X-ray diffraction and solid-state NMR spectroscopy. All the layered silicates studied were found to be able to generate a $Lu_2Si_2O_7$ phase after hydrothermal treatment

* e-mail address of the corresponding author: alba@icmse.csic.es

under subcritical conditions, thereby confirming the participation of a chemical mechanism of the clay barrier generating phases being stables with temperature and pH conditions. However, the extent of this reaction depends to a large extent on the physicochemical properties of the framework and the interlayer space composition, such as the presence or absence of an octahedral sheet, the degree of occupancy of this sheet, and the origin and total layer charge. Therefore, this study allows tuning the clay mineral framework characteristic that favors the rare earth cations (as trivalent actinide simulator) immobilization.

Key Words—Bentonite, smectite, Engineered barrier, disilicates, rare-earth, hydrothermal treatment, subcritical conditions, X-ray diffraction, MAS-NMR, radioactive waste.

1. Introduction

High-level actinide-containing radioactive waste has become a key environmental problem with the development of nuclear energy as a safe and efficient approach for long-term waste storage must be found. A deep geological repository (DGR) based on an engineered and natural multibarrier system is considered to be the most promising method for the management of long-lived nuclear waste (Savage and Chapman., 1982). However, the radionuclides stored in a DGR may reach the geosphere and the biosphere in the long-term as a result of groundwater-induced dissolution of the canister and subsequent upward transport by the water through the barriers and host rock. The most efficient way to enhance radionuclide retention by sorption involves the construction of engineered barriers, which are usually composed of clays (Meunier et al., 1998). Within the DGR, clay-engineered barriers, which are usually placed between the metal canister containing the radioactive

waste and external concrete barriers, play a major role in radionuclide retention. The clay minerals used tend to have low permeability and diffusivity, a high sorption capacity, and strong buffering properties (Meunier et al., 1998; Landais, 2006; Itakura et al., 2010). Smectites (the main constituent of the bentonites) are generally considered to be the most efficient of the clays used for this purpose due to their ability to undergo strain without fracturing, their low hydraulic conductivity, high cation sorption capacity, and their ability to expand and enter into close contact with both waste and rock (Pusch, 2006). However, both the physical and chemical nature of smectites is a key issue in the design of these barriers as factors related to their microstructure and chemical properties, such as clay geometry and isomorphic substitutions, may affect radionuclide sorption (Galunin et al., 2010).

Groundwater infiltration, which can transport the radionuclides in dissolved form or as colloids or small particles, is one of the main handicaps to be overcome during the design and construction of safe nuclear waste repositories. Thus, if the water reaches the canister and corrodes it, the barrier system should be able to retain the radionuclides in the water and avoid their transport away from the repository (Cuadros, 2008). Interaction of this barrier material with groundwater can, however, modify its physical and chemical properties, thus decreasing its groundwater isolation capacity or, in the case of canister failure, decreasing the radionuclide retention capacity of clay materials (Pusch et al., 2007). Loss of the swelling and the cationic-exchange capacity of these materials under DGR conditions has been well studied (Jennings and Thompson, 1986; Eberl et al., 1993; Cuadros and Linares, 1996) and is recognized to be the main drawback to the use of bentonite in DGRs (Meunier et al., 1998; Bauer et al., 2001). In light of this, an alternative and effective immobilization mechanism could involve the chemical retention of actinides

by bentonite. This assumption is supported by studies of Perdigón (2002) and Alba and Chaín (2005, 2007), who demonstrated that lutetium disilicate ($Lu_2Si_2O_7$) forms when a nitric acid solution of lutetium reacts with saponite under pressures and temperatures similar to those found in a DGR, even after weathering of the smectite. Moreover, the persistence of $Lu_2Si_2O_7$ under hydrothermal conditions covering a wide range of pH and different salt solutions has been demonstrated (Alba and Chain, 2007). Disilicate-phase synthesis has therefore been proposed to be a possible long-term retention solution for trivalent actinide cations.

To ensure optimal trivalent radioactive cation immobilization by chemical interaction, it is important to understand the structural properties of smectites that enhance their reactivity with Ln^{3+} ions and lead to formation of the disilicate phase. This information could be extremely useful in finding smectites that yield the disilicate phase under even milder conditions than those already reported, and would be especially relevant to the design of effective repositories for high-level radioactive waste.

The main aim of this paper is to characterize the formation of $Lu_2Si_2O_7$ from a set of different phyllosilicates upon treatment with a Lu^{3+} solution under subcritical conditions and to establish the chemical and structural characteristics of these phyllosilicates that favor this chemical reaction. Although Lu^{3+} is not the best lanthanide mimic of the trivalent actinides most commonly found in high activity radioactive waste (Np, Am, and Cm) (Astudillo, 2001), it is has been chosen because Alba et al. (2009) have shown that the formation of rare-earth disilicates is common to all rare earths, with lutetium being the most reactive.

2. Materials and methods

2.1. Materials

One of the seven well-characterized phyllosilicates selected for this study (structural formulae are shown in Table 1) was a 1:0 phyllosilicate (with only a tetrahedral sheet, T), whereas the remainder had a 2:1 layer structure (T-O-T structure). The 1:0 phyllosilicate selected was a synthetic kanemite, $Na[Si_2O_4(OH)].3H_2O$, which is a layered silicate containing only one sheet of orthosilicate tetrahedra. The orthosilicate groups are condensed into three of its vertices (Q^3) in an irregular hexagonal arrangement. The silicate sheets are bound by hydrogen bonds, and hydrated Na^+ cations that interact strongly with the hydroxyl groups of the sheets are found in the interlayer space. A more detailed structural description of this silicate can be found elsewhere (Alba et al., 2006). The selected 2:1 phyllosilicates include a dioctahedral and a trioctahedral layered silicate, which are almost free of no substitutional charge (pyrophyllite and talc respectively), three trioctahedral smectites (saponite, hectorite, and Laponite®), and one trioctahedral vermiculite, namely eucatex (Williams-Daryn et al., 2002). Two of these silicates (vermiculite and saponite) contain Al substituting for Si in the tetrahedral sheet of the clay, whereas the rest contain only Si in the tetrahedral sheet. Hectorite and Laponite® contain Li substituting for Mg in the octahedral sheet and differ in their degree of crystallization, which is poorer in Laponite® than in hectorite. Original samples with particle diameters of less than 2 μm were used after removal of carbonates and organic matter.

Finally, a Na-hectorite was prepared by ion-exchange according to the method described by Miller et al. (1982).

121

122 *2.2. Hydrothermal treatments*

123

124 A 300 mg sample of the powdered silicate and 50 mL of $7.3 \cdot 10^{-2}$ M
125 $Lu(NO_3)_3 \cdot 3.6H_2O$ solution were transferred into a stainless steel T316SS hydrothermal
126 reactor and heated to 300º C for 48 hours under autogenous pressure. After this time the
127 reactor was cooled to room temperature and the solids separated by filtration, washed
128 repeatedly with distilled water, and allowed to dry in air at 25ºC. Although geochemical
129 waste degradation and waste/rock interaction processes in the hydrothermal environment
130 remain predictable up to temperatures of to about 200º C, many studies devoted to
131 simulating deep geological disposal conditions use temperatures of up to 350º C to increase
132 the reaction rates (Mather et al., 1982; Savage and Chapman, 1982; Allen and Wood, 1988;
133 Alba and Chain, 2007). The low solid/liquid ratio has been used in accordance with
134 previous related works (Alba and Chain, 2005; Alba et al., 2009; Galunin et al., 2009;
135 2010; 2011) and to allow performing the comparison of the results.

136

137 *2.3. Characterization*

138 *2.3.1. X-ray powder diffraction (XRD).*

139 XRD patterns were obtained using a Bruker D8I instrument at CITIUS (Centre of
140 Research, Technology and Innovation of Seville University), University of Seville (Spain).
141 This diffractomer works with a Ni-filtered Cu K_α radiation, at 40 kV and 40 mA.
142 Diffractograms were obtained from 3 to 70° 2θ at a scan step of 0.05° 2θ and with a
143 counting time of 3 s.

144

145 *2.3.2. NMR spectroscopy (MAS NMR).*

146 ^{29}Si, ^{27}Al, and ^{1}H single-pulse spectra were recorded using a Bruker DRX400
147 spectrometer with a magnetic field of 9.36 T and equipped with a multinuclear probe by the
148 Spectroscopy Service at ICMS (Material Science of Seville, CSIC-US). Powdered samples
149 were packed in 4 mm zirconia rotors and spun at 12 kHz. ^{1}H MAS NMR spectra were
150 obtained at a frequency of 400.13 MHz using a typical $\pi/2$ pulse width of 4.5 μs and a delay
151 time of 5 s. ^{29}Si MAS NMR spectra were obtained at a frequency of 79.49 MHz using a
152 pulse width of 2.7 μs ($\pi/2$ pulse length = 8.1 μs) and a delay time between 60 and 600 s.
153 ^{27}Al MAS NMR spectra were recorded at 104.26 MHz with a pulse width of 1.1 μs ($\pi/2$
154 pulse length = 11.0 μs) and delay time of 3 s. Chemical shifts are reported in ppm with
155 respect to tetramethylsilane for ^{29}Si and ^{1}H and a 0.1 M solution of $AlCl_3$ for ^{27}Al. All
156 spectra were simulated using a modified version of the Bruker Winfit program to handle the
157 finite spinning speed in MAS experiments (Massiot et al., 2002). A Gaussian–Lorentzian
158 model was used for all peaks. The fitted parameters were intensity, position, line-width, and
159 Gaussian/Lorentzian ratio.

160

161

162 **3. Results**

163 *3.1. Phyllosilicates with no substitutional charge*

164

165 The XRD pattern of kanemite (Fig. 1a) consisted of a set of reflections
166 corresponding to those of the standard kanemite structure PDF 25-1309 with a *020* basal
167 spacing of 10.2 Å (Johan and Maglione, 1972). All these reflections disappeared after
168 hydrothermal treatment in Lu^{3+} solution (Fig. 1b) to give a pattern similar to that of

169 $Lu_2Si_2O_7$ (PDF 35-0326) with small reflections corresponding to the secondary phases
170 tridymite (PDF 18-1170) and $H_2Si_2O_5$ (PDF 74-1548).

171 The XRD pattern of pyrophyllite (Fig. 1a) was indexed according to the PDF 46-
172 1308 pattern, with a basal spacing of 9.1 Å. Hydrothermal treatment in Lu^{3+} solution (Fig.
173 1b) did not alter the structure, crystallinity, or the collapsed state of the layers, which
174 maintained the basal spacing of the starting material. The emergence of a new reflection at
175 14.6 º 2θ was observed in the XRD pattern corresponding to boehmite (PDF 76-1871),
176 which was previously observed as a product of hydrothermal treatment of pyrophyllite
177 under aqueous acidic conditions at 300ºC (Alba et al., 2010), thus indicating that this
178 structure shows some stability under hydrothermal conditions (Bentabol et al., 2003). The
179 whole set of reflections for the $Lu_2Si_2O_7$ phase was also evident alongside some minor
180 reflections for the $H_2Si_2O_5$ phase.

181 The XRD pattern of talc (Fig. 1a) was indexed according to PDF 29-1494, with a
182 basal spacing of 9.2 Å due to the non-swelling layered silicate. The presence of talc in the
183 XRD pattern of the treated sample (Fig. 1b) was minor, with the diffractogram being
184 dominated by the $Lu_2Si_2O_7$ phase. No other secondary phases arising from the
185 decomposition of talc were detected.

186 Analysis of the samples by MAS NMR spectroscopy was carried out to determine
187 the presence of any change in short-range order. The ^{29}Si MAS NMR spectra of the starting
188 materials and those obtained after hydrothermal treatment (Fig. 2, Table 2) revealed a
189 typical single signal centered at -97.3 ppm for kanemite due to the existence of Q^3 silicon
190 tetrahedra (Blasco et al., 1995). The spectra for treated samples show three signals at -91.8,
191 -100.5, and -111.5 ppm. The absence of a signal at -97.3 ppm indicates the absence of a Si
192 environment typical of kanemite. The most intense signal at -111.5 ppm was assigned to

193 the Q^4(0Al) environment of tridymite, which presents a set of signals between -109.0 and -
194 113.0 ppm with a maximum at -111.0 ppm (Engelhardt and Michel, 1987). The signal at -
195 91.8 ppm corresponds to the Q^1 environment of $Lu_2Si_2O_7$ (Alba et al., 2001a; 2001b) and
196 implies a transformation of 11.4% of kanemite to this phase. Finally, the minor contribution
197 at -100.5 ppm was assigned to $H_2Si_2O_5$ (Heidemann et al., 1985). This finding is in good
198 agreement with the XRD data. The transformation of kanemite after hydrothermal reaction
199 was also evident in the ^{1}H MAS NMR spectra (Fig. 2 right). Thus, the ^{1}H MAS NMR
200 spectrum of the initial sample contains two broad signals, one at 4.80 ppm, which was
201 assigned to hydroxyl groups and free interlayer water, and the other at 14.80 ppm due to
202 water involved in the bridging hydrogen bonds (Alba et al., 2006). Only a narrow signal at
203 4.70 ppm, which could be assigned to hydration water of the $Lu_2Si_2O_7$ and $H_2Si_2O_5$ phases,
204 was observed after the hydrothermal treatment (Perdigón, 2002).

205 The ^{29}Si NMR spectrum of pyrophyllite (Fig. 2, Table 2) shows a signal at -95.2
206 ppm corresponding to a Q^3 coordination sphere with no Al atoms in the neighboring
207 tetrahedra (Q^3(0Al); Engelhardt and Michel, 1987). The spectra recorded after
208 hydrothermal treatment show a contribution in the same position as for the untreated
209 sample, along with two minor contributions due to $Lu_2Si_2O_7$ and $H_2Si_2O_5$ in a proportion of
210 4.3 % and 1.8 %, respectively. The ^{1}H MAS NMR spectra of untreated and treated
211 pyrophyllite show a single signal at 2.19 ppm, as could be expected for the ^{1}H resonance
212 signal of the hydroxyl group in dioctahedral 2:1 phyllosilicates (Alba et al., 2003). The ^{27}Al
213 MAS NMR spectra (not shown) of the untreated pyrophyllite (the only sample with
214 framework Al) and that recorded after the hydrothermal treatment were found to be
215 identical, with a single peak at ~0 ppm due to the octahedral Al environments (Engelhardt
216 and Michel, 1987). These results again suggest the stability of the pyrophyllite structure

after treatment. The formation of boehmite upon treatment of pyrophyllite produced no spectral changes due to the octahedral coordination of Al in this phase (Engelhardt and Michel, 1987).

Finally, talc showed a single contribution in the ^{29}Si MAS NMR spectrum at -98.1 ppm due to Q^3(0Al) (Sanz and Serratosa, 1984). The main peak (-91.7 ppm) in the spectrum of the hydrothermally treated sample (83.6%) corresponds to the Q^1 environment of $Lu_2Si_2O_7$. The remaining talc ^{29}Si signal at -97.7 ppm was found to be shifted towards higher frequency (higher ppm value) upon hydrothermal treatment, possibly as a result of vacancies in the octahedral sheet generated by Mg^{2+} leaching (Luce and Park, 1972; Sanz and Serratosa, 1984; Corma et al., 1987). Mg^{2+} leaching from the octahedral sheet during treatment was also evident from the shift of the hydroxyl ^{1}H NMR signal (Fig. 2b, right) towards higher frequency (Alba et al., 2003). The ^{1}H MAS NMR spectrum of the treated talc also shows a signal at 4.74 ppm due to hydration water of the $Lu_2Si_2O_7$ phase (Perdigón, 2002).

3.2. Charged phyllosilicates

Structural changes in the long-range order of the charged trioctahedral 2:1 phyllosilicates after hydrothermal treatment were analyzed by XRD (Fig. 3 and 4). All the reflections observed for the initial samples (Fig. 3a and 4a) were consistent with the general and basal reflections of smectite and vermiculite, except the reflection at around 30º 2θ in hectorite, which corresponds to cristobalite (PDF 03-272). The *060* reflections were observed at a 2θ angle that corresponds to a distance of 1.51-1.53 Å between the reflection planes, which is typical of trioctahedral 2:1 phyllosilicates (Grim, 1968). The *001* basal

241 reflection corresponds to a d_{001} value of around 12.0 Å and was assigned to a water
242 monolayer around the interlayer cations (Alba et al., 2001a). The XRD pattern of Laponite®
243 showed broader reflections than the other silicates, mainly due to its smaller particle size,
244 which causes a relative loss of long-range order, and probably due to a mixed hydration
245 state (Wheeler et al., 2005).

246 In general, a complete absence of *hkl* reflections (Fig. 3b and 4b) is observed after
247 the hydrothermal treatment, thus indicating disruption of the basic structure of the silicates.
248 Indeed, except for vermiculite, hydrothermal treatment caused a partial swelling of the
249 layers due to the total replacement of the original interlayer cations by the trivalent cation
250 Lu^{3+} (Alba et al., 2001a). The number and intensity of the basal reflections decreased,
251 probably because of a lower-order stacking of the layers after treatment.

252 The emergence of small reflections corresponding to $Lu_2Si_2O_7$ was evident in both
253 hectorites (natural and homoionized in Na^+) after hydrothermal treatment (Fig. 3b). The
254 XRD pattern of the treated Na-hectorite was dominated by the crystalline phases of β-
255 cristobalite (PDF 89-3607) and enstatite (PDF 73-1937), which were accompanied by
256 minor reflections due to $H_2Si_2O_5$. No crystalline secondary phases were observed in the
257 XRD pattern of the treated hectorite, which only exhibited a broad signal in the range 20–
258 35º 2θ due to the amorphous phase. The XRD pattern of treated Laponite® (Fig. 3b) only
259 showed reflections due to $Lu_2Si_2O_7$.

260 The XRD patterns of the treated saponite and vermiculite (Fig. 4b) were dominated
261 by $Lu_2Si_2O_7$, although other minor phases were also observed. Natrosilite (PDF 23-0529)
262 and $H(Mg_2(SiO_4))_8$ (PDF 87-2051) were formed in both samples, and kaolinite (PDF 78-
263 1996) and $Mg_{10}(Si_3O_{14})(OH)_4$ (PDF 81-544) were also observed in vermiculite.

The changes in short-range order produced by the hydrothermal treatment were followed by MAS NMR spectroscopic analysis of the active nuclei present in each silicate (Fig. 5–7 and Tables 3 and 4). The only major signal in the ^{29}Si MAS NMR spectrum of untreated hectorites (Table 3) was a peak in the range of chemical shifts associated with the Q^3 (0Al) environment at -95.0 ppm. The shift of this signal to higher frequencies with respect to talc is due to the isomorphic substitution of Li^+ for Mg^{2+} in the octahedral sheet, which resulted in a decrease in the electronegativity of the cations coordinated by the apical oxygen of the tetrahedral sheet (Weiss et al., 1987). Hydrothermal treatment resulted in more complex ^{29}Si MAS NMR spectra for both hectorites. These spectra were deconvoluted into six contributions (see Table 3). The signals for both these samples corresponded to similar environments but with different relative intensities. The main differences can be summarized as follows: (i) the Q^3(0Al) signal of the remaining hectorite was 27.1% in the natural hectorite and 5.8% in the Na-hectorite; (ii) the Q^1 environment of $Lu_2Si_2O_7$ (-91.7 ppm) was 13.3% and 12.7%, respectively; (iii) a signal at -79.8 ppm assigned to the Q^0 environment of X_2-Lu_2SiO_5 (16.4%; Becerro et al., 2004), which was absent in the Na-hectorite, was observed in the natural sample; and (iv) the other signals at around -85 ppm, -101 ppm, and -111 ppm corresponded to the secondary phases enstatite (Mägi et al., 1984), H_2SiO_5 (Heidemann et al., 1985) and β-cristobalite (Smith and Blackwell, 1983), which together contributed a total of 43.2% and 81.5%, respectively.

The initial spectrum of Laponite® (Table 3) was characterized by a main signal at -94.5 ppm, which was assigned to a Q^3(0Al) environment, along with a shoulder at -97.3 ppm and a minor peak at -85.2 ppm. The main signal shifted to higher frequency with respect to that for hectorite due to the increased layer-charge deficit in Laponite® (Weiss et al., 1987). The signal at -97.3 ppm was due to the presence of partially condensed Si

tetrahedra with anionic basal oxygens, in other words $(SiO)_3SiO^-$ (Wheeler et al., 2005), whereas the higher-frequency signal was assigned to silanol groups, namely $(SiO)_3SiOH$ (Weiss et al., 1987; Wheeler et al., 2005). The signals of the original spectrum disappeared after hydrothermal treatment and two new signals, corresponding to δ-$Na_2Si_2O_5$ (Mortuza, 1989) and $Lu_2Si_2O_7$, appeared at -90.6 ppm (27.2%) and -91.7 ppm (72.8%), respectively.

The ^{29}Si MAS NMR spectrum of the untreated saponite showed a signal with three contributions (Table 4): an intense signal at -95.8 ppm and two lower-intensity signals at -90.8 and -85.0 ppm, corresponding to Q^3(0Al), Q^3(1Al), and Q^3(2Al) Si environments, respectively (Alba et al., 2001b). Calculation of the Si/Al ratio gave a value of 8.4, which agrees well with the theoretical value of 9.0 obtained from the chemical formula. The treated sample exhibited a ^{29}Si MAS NMR spectrum containing four signals. The remaining saponite showed only a single ^{29}Si contribution at -95.0 ppm (2.4%) due to the Q^3(0Al) Si environment, thus indicating that hydrothermal treatment results in the absence of Q^3(1Al) and Q^3(2Al) Si environments, possibly due to partial leaching of Al from the tetrahedral sheet. The other three new signals are found at -91.7, -88.5, and -72.5 ppm and correspond to $Lu_2Si_2O_7$ (71.4%), natrosilite (Alba and Chain, 2005), and the Q^1 Si environments of $H(Mg_2(SiO_4))_8$ (Engelhardt and Michel, 1987; Haiber et al., 1997).

The ^{29}Si NMR signals obtained for vermiculite (Table 4) were abnormally broad due to the presence of Fe in its structure. Thus, the single signal with a maximum at -88.5 ppm, due to Q^3 environments, observed for the untreated sample could be fitted to four peaks (Table 4). The small Si/Al ratio in this silicate (3.5) resulted in a greater contribution of Q^3(mAl) with $m \neq 0$ environments to the ^{29}Si signal than in the saponite sample. The signals corresponding to the vermiculite disappeared after hydrothermal treatment and the ^{29}Si MAS NMR spectrum was composed of three new signals at -91.4, -88.2, and -76.3

312 ppm, which were assigned to $Lu_2Si_2O_7$ (57.9%), natrosilite, and the Q^1 and Q^0 Si
313 environments of the magnesium silicate phases (Pacalo and Parise, 1992; Haiber et al.,
314 1997) observed by XRD.

315 The ^{1}H MAS NMR spectra of the untreated smectites (Fig. 5 and 6, right) showed
316 two well-resolved peaks, one in the range 0.30-0.65 ppm, which was assigned to
317 framework hydroxyl groups, and the other in the range 3.70-4.30 ppm, which was assigned
318 to interlayer water. The position of both signals was found to depend on the chemical
319 composition of the smectite (Alba et al., 2003). In general, hydrothermal treatment resulted
320 in a shift of the hydroxyl signal to greater frequency, as observed previously when
321 vacancies in the octahedral sheet were produced by leaching of framework cations (Alba et
322 al., 2003). This treatment also caused the water signal to shift to higher frequency due to
323 replacement of the Na^+ or Ca^{2+} interlayer cation by framework Mg^{2+}, Al^{3+}, or Lu^{3+} from the
324 solution (Alba et al., 2003). Moreover, the water signals were found to be broader after
325 treatment due to the miscellaneous composition of the interlayer space. The ^{1}H MAS NMR
326 spectra of the untreated and treated vermiculite did not allow the two expected proton
327 environments to be resolved due to the amount of paramagnetic impurities present in the
328 silicate, thus meaning that these spectra were of little analytical value.

329 A ^{27}Al MAS NMR study was only carried out for the aluminum silicates saponite
330 and vermiculite (Fig. 7), both of which showed a single signal at around 60 ppm due to
331 tetrahedral Al (Engelhardt and Michel, 1987). The hydrothermal treatment of both samples
332 resulted in the appearance of a new signal at around 0 ppm due to octahedral Al
333 (Engelhardt and Michel, 1987) and disappearance of the signal at around 60 ppm as a result
334 of Al leaching from the tetrahedral sheet. These findings are in good agreement with the

disappearance of the Q^3(mAl) with m≠0 environments from the ^{29}Si MAS NMR spectra after treatment.

4. Discussion

The XRD and NMR results show that the 1:0 and 2:1 phyllosilicates are chemically suitable for $Lu_2Si_2O_7$ formation.

An analysis of the results for kanemite, pyrophyllite, and talc allow the role of the octahedral layer in the generation of lutetium disilicate to be defined. Likewise, the order of reactivity can be extracted from the contribution of the Q^1 Si environment ($Lu_2Si_2O_7$) to the ^{29}Si MAS NMR spectra, with talc being the most reactive (83.6%), followed by kanemite (11.4%), and, finally, pyrophyllite (4.3%). As can be seen from the XRD results, the higher hydrothermal stability of trioctahedral silicates with respect to their dioctahedral counterparts in neutral and acidic media (Alba et al., 2010) could favor the permanence of the laminar structure before the reaction with lutetium, and thus a suitable environment for generating the disilicate phase (Becerro et al., 2003). The laminar structure of the silicate has been shown to be the main factor favoring disilicate phase generation, thus meaning that the SiO_2 as a source of silicon is unable to produce disilicates under hydrothermal conditions (Perdigón, 2002).

The results obtained for kanemite are more difficult to interpret as two competing factors participate in the process. Thus, the absence of an octahedral sheet confers a high flexibility to the layers, thereby allowing this material to be used as a precursor for the synthesis of a large number of compounds (Kooli, 2002; Selvam et al., 2003) that could evolve towards stable structures under hydrothermal conditions. However, this same

358 flexibility is accompanied by a low hydrothermal stability that results in the evolution of Q^3
359 environments towards Q^4 condensation and therefore lower reactivity (Perdigón, 2002).
360 The layer charge in 2:1 phyllosilicates results from isomorphic substitutions in the
361 tetrahedral or octahedral sheets. The influence of this layer charge can be determined by
362 comparing the reactivity of saponite and hectorite/Laponite®. Thus, saponite and
363 Laponite® present a higher reactivity as regards the formation of RE disilicate (71.4% and
364 72.8%, respectively), followed by hectorite (13.3%). The marked difference in reactivity
365 between saponite and hectorite in favor of the former is due to substitutions in the
366 tetrahedral sheet rather than in the octahedral layer (Alba et al., 2001a; 2001b). Thus, Li^+
367 leaches more easily than Mg^{2+} from the octahedral sheet and the latter leaches more easily
368 than Al^{3+} from the tetrahedral sheet. This is evident upon comparing the XRD diffraction
369 patterns of hectorite and saponite, with the former being compatible with the presence of
370 most of the components as an amorphous phase, whereas the persistence of the *001*
371 reflection in the saponite XRD pattern is compatible with the presence of hydrated Lu^{3+}
372 and/or Al^{3+} in the interlayer space. The marked difference in reactivity between Laponite®
373 and hectorite, which have a similar origin and layer charge, is due to the smaller particle
374 size in Laponite® (Wheeler et al., 2005). This smaller particle size and the largest number
375 of structural defects improve the reaction kinetics since this reaction follows a
376 reconstructive reaction mechanism (Archilla et al., 2006).
377 The influence of the layer charge on the hydrothermal reactivity can be studied by
378 comparing the results obtained for saponite and the vermiculite eucatex, with the main
379 difference between the two being the higher layer charge of the vermiculite. The formation
380 of $Lu_2Si_2O_7$ is higher for saponite (71.4%) than for vermiculite (57.9%), thus apparently
381 contradicting the observed guideline whereby substitutions in the tetrahedral sheet increase

382 the reactivity. Therefore, the main responsible for this reactivity order may be the highest
383 hydrothermal stability of the saponite versus vermiculite, as previously reported by Alba et
384 al. (2010). A possible explanation for this finding is that an increase in the number of
385 substitutions in the tetrahedral sheet favors the leaching of Al^{3+} cations, which in turn leads
386 to disintegration of the structure to form a more stable and less reactive phase, like
387 kaolinite. This is also reinforced by the greater reactivity shown by talc, which is a neutral
388 trioctahedral layered silicate.

389 Finally, analysis of the effect of the interlayer cation on the synthesis is based on the
390 results obtained from hectorites (natural Ca-hectorite and homoionized with Na^{+}). Both
391 these materials display a similar hydrothermal reactivity as regards $Lu_2Si_2O_7$ formation (ca.
392 13%) but with an important difference in terms of hydrothermal stability in favor of the
393 natural hectorite (the remaining Q^3(0Al) contribution was 27.1% and 5.8%, respectively).
394 The long-range order is lost in both cases, as observed by XRD. In addition, the degree of
395 crystallization of secondary products is more advanced in the Na-hectorite. Finally, the
396 presence of X_2-Lu_2SiO_5, which has previously been detected as a degradation product when
397 Ca is present in the reaction medium, was observed for the natural hectorite (Alba and
398 Chain, 2007).

399

400 **5. Conclusions**

401

402 All the layered silicates studied are able to generate a $Lu_2Si_2O_7$ phase after
403 hydrothermal treatment under subcritical conditions, thus demonstrating the additional
404 chemical immobilization mechanism of the clay barrier. However, the extent of this

405 reaction depends on the presence or absence of an octahedral sheet, the degree of
406 occupancy of this sheet, and the total layer charge and its origin.

407 In the context of engineered-barrier safety, the structure of the selected bentonite
408 must fulfill the following conditions: 2:1 layer stacking (T-O-T structure) with complete
409 occupancy of the octahedral sheet, the absence of octahedral isomorphic substitutions, and
410 a moderate tetrahedral isomorphic substitution of Al for Si. As a secondary factor, sodium
411 is preferred to calcium as an interlayer cation because the presence of calcium in the
412 medium favors the formation of the Lu_2SiO_5 vs $Lu_2Si_2O_7$, a most stable phase. These
413 requirements provide a higher hydrothermal reactivity.

414

415 ## Acknowledgements

416 We gratefully acknowledge financial support from DGICYT and FEDER funds (Projects CTQ2010-14874).

417 ## References

418 Alba, M.D., Becerro, A.I., Castro, M.A., Perdigón A.C, 2001a. Hydrothermal reactivity of Lu-saturated
419 smectites: Part I. A long-range order study. American Mineralogist 86, 115-123.

420 ——— 2001b. Hydrothermal reactivity of Lu-saturated smectites: Part II. A short-range order study.
421 American Mineralogist 86, 124-131.

422 Alba, M.D., Becerro, A.I., Castro, M.A., Perdigón, A.C., Trillo, J.M., 2003. Inherent acidity of aqua metal
423 ions in solids: assay in layered aluminosilicates. Journal of Physical Chemistry B 107, 3996-4001.

424 Alba, M.D., Castro, M.A., Chain, P., Orta, M.M, Pazos, M.C., Pavon, E., 2010. Hydrothermal stability of
425 layered silicates in neutral and acidic media: Effect on engineered-barrier safety. Clays and Clay
426 Minerals 4, 501-514.

427 Alba, M.D., Chain, P., 2005. Interaction between Lutetium Cations and 2:1 Aluminosilicates under
428 Hydrothermal Treatment. Clays and Clay Minerals 53, 39-46.

——— 2007. Persistence of lutetium disilicate. Applied Geochemistry 22, 192-201.

Alba, M.D., Chain, P., Orta, M.M., 2009. Chemical reactivity of argillaceous material in engineered barrier Rare earth disilicate formation under subcritical conditions. Applied Clay Science 43, 369-375.

Alba, M.D., Chain, P., Pavón E., 2006. Synthesis and characterization of gallium containing kanemite. Microporous and Mesoporous Materials 94, 66-73.

Allen, C.C., Wood, M.I., 1988. Bentonite in Nuclear Waste Disposal: A Review of Research in Support of the Basalt Waste Isolation Project. Applied Clay Science 3, 11-30.

Ames, L.L., Sand, L.B., Goldich, S.S., 1958. A contribution on the Hector, California bentonite deposit. Economic Geology 53, 22-37.

Archilla, J.F.R., Cuevas, J., Alba, M.D., Naranjo, M., Trillo, J.M., 2006. Discrete breathers for understanding reconstructive mineral processes at low temperature. Journal of Physical Chemistry B 110, 24112-24120.

Astudillo, J., 2001. "El almacenamiento geológico profundo de los residuos radiactivos de alta actividad. Principios básicos y tecnología.", Editorial ENRESA.

Bauer, A., Scäfer, T., Dohrmann, R., Hoffmann, H., Kim, J.J., 2001. Smectite stability in acid salt solutions and the fate of Eu, Th and U in solution. Clay Mineral 36, 93-103.

Becerro, A.I., Naranjo, M., Perdigón, A.C., Trillo, J.M., 2003. Hydrothermal chemistry of silicates: low-temperature synthesis of *y*-Yttrium disilicate. Journal of American Ceramic Society 86, 1592-1594.

Becerro, A.I., Escudero, A., Florian, P., Massiot, D., Alba, M.D., 2004. Revising $Y_2Si_2O_7$ and Y_2SiO_5 polymorphic structures by ^{89}Y MAS-NMR spectroscopy. Journal of Solid State Chemistry 177, 2783-2789.

Bentabol, M., Cruz, M.D.R., Huerta, F.J., Linares, J., 2003. Hydrothermal transformation of kaolinite at 200 and 300 degrees C. Clay Minerals 38, 161-172.

Blasco, T., Corma, A., Navarro, M.T., Pariente, J.P., 1995. Synthesis, characterization, and catalytic activity of Ti- MCM-41 structures. Journal of Catalysis 156, 65-74.

Corma, A., Mifsud, A., Sanz, E., 1987. Influence of the chemical composition and textural characteristic of palygorskite on the acid leaching of octahedral cations. Clay Minerals 22, 225-232.

Cuadros, J., 2008. Clays as sealing material in nuclear waste repositories. Geology Today 24, 90-103.

457 Cuadros, J., Linares, J., 1996. Experimental Kinetic study of the smectite-illite transformation. Geochimica et
458 Cosmochimica Acta, 60, 439-453.
459 Eberl, D.D., Velde, B., McCormick, T., 1993. Synthesis of illite-smectite from smectite at earth surface
460 temperatures and high pH. Clay Minerals 28, 49-60.
461 Engelhardt, G., Michel, D. (editors), 1987. High-resolution Solid-State NMR of Silicates and Zeolites. John
462 Wiley & Sons, New York.
463 Galunin, E., Alba, M.D., Aviles, M.A., Santos, T., Vidal, M., 2009. Reversibility of la and Lu sorption onto
464 smectites: Implications for the design of engineered barriers in deep geological repositories. Journal of
465 Hazardous Materials 172, 1198-1205.
466 Galunin, E., Alba, M.D., Santos, M.J., Abrao, T., Vidal, M., 2010. Lanthanide sorption on smectitic clays in
467 presence of cement leachates. Geochimica et Cosmochimica Acta 74, 862-875.
468 Galunin, E., Alba, M.D., Santos, M.J., Abrao, T., Vidal, M., 2011. Examination of competitive lanthanide
469 sorption onto smectites and its significance in the management of radioactive waste. Journal of
470 Hazardous Materials 186, 1930-1941.
471 Grim, R.E., 1968. Clay Mineralogy: McGraw-Hill Book Company, New York.
472 Haiber, M., Ballone, P., Porinello, M., 1997. Structure and dynamics of protonated Mg_2SiO_4: An ab-initio
473 molecular dynamics study. American Mineralogist 82, 913-922.
474 Heidemann, D., Grimmer, A.R., Hübert, C., Starke, P., Mägi, M., 1985. Solid-state high-resolution Si-29
475 NMR-studies of polycrystalline phyllosilicic acids $(H_2Si_2O_5)_x$ at low and high magnetic-field.
476 Zeitschrift für Anorganische und Allgémeine Chemie 528, 22-36.
477 Itakura, T., Airey, D.W., Leo, C.J., Payne, T., McOrist, G.D., 2010. Laboratory studies of the diffusive
478 transport of Cs-137 and Co-60 through potential waste repository soils. Journal of Environmental
479 Radioactivity 101, 723-729.
480 Jennings, S., Thompson, G.R., 1986. Diagenesis of Pilo-Pleistocene sediments of the Colorado River Delta,
481 southern California. Journal of Sedimentary Petrology 56, 89-98.
482 Johan, Z., Maglione, G.F., 1972. Kanemite a new hydrated sodium silicate. Bulletin de la Societé Française
483 Mineralogie et de Cristallographie 95, 371-382.

Kooli, F., 2002. Recrystallization of a new layered silicate from Na-kanemite-tetramethylammonium hydroxide-water-,4-dioxane mixture. Journal of Materials Chemistry 12, 1374-1380.

Landais, P., 2006. Advances in geochemical research for the underground disposal of high-level, long-lived radioactive waste in a clay formation. Journal of Geochemical Exploration 88, 32-36.

Laporte Industries Ltd. (1990) Laponite Technological Bulletin, L104/90/A, 1.

Levitz, P., Lecolier, E., Mourchid, A., Delville, A., Lyonnard, S., 2000. Liquid-solid transition of laponite suspension at very low ionic strength: Long-range electrostatic stabilization of anisotropic colloids. Europhysiscs Letters 49, 672-677.

Luce, R.W, Parks, G.A., 1972. Dissolution kinetics of magnesium silicates. Geochimica et Cosmochimica Acta 36, 35-50.

Mägi, M., Lippmaa, E., Samoson, A., 1984. Solid-State High-Resolution Si-29 Chemical-Shift in Silicates. Journal of Physical Chemistry 88, 1518-1522.

Massiot, D., Fayon, F., Capron, M., King, I., Le Calvé, S., Alonso, B., Durand, J.O., Bujoli, B., Gan, Z., Hoatson, G., 2002. Modelling one- and two-dimensional solid-state NMR spectra. Magnetic Resonance in Chemistry 40, 70-76.

Mather, J.D., Chapman, N.A., Black, J.H., Lintern, B.C., 1982. The geological disposal of high-level radioactive waste-a review of the Institute of Geological Sciences Research programme. Nuclear Energy 21, 167-173.

Meunier, A., Velde, B., Griffault, L., 1998. The reactivity of bentonites: a review. An application to clay barrier stability for nuclear waste storage. Clays and Clay Minerals 33, 187-196.

Miller, S.E., Heath, G.R., González, R.D., 1982. Effects of Temperature on the Sorption of Lanthanides by Montmorillonites. Clays and Clay Minerals 30, 111–122.

Mortuza, M.G., 1989. A Nuclear Magnetic Resonance Investigation of the Structure of Some Alkali Silicate Glasses. PhD Thesis, University of Warwick.

Pacalo, R.E.G., Parise, J.B., 1992. Crystal-Structure of Superhydrous-B, a Hydrous Magnesium-Silicate Synthesized at 1400-Degrees-C and 20-GPa. American Mineralogist 77, 681-684.

Perdigón, A.C., 2002. Estudio del sistema saponita/$Lu(NO_3)_3/H_2O$ en condiciones hidrotérmicas. Ph.D.thesis, University of Seville, Seville (Spain).

512 Petit, S., Martin. F., Wiewiora. A., De Parseval, P., Decarreau, A., 2004. Crystal-chemistry of talc: A near
513 infrared (NIR) spectroscopy study. American Mineralogist 89, 319-326.
514 Prost, J.L., 1984. Saponite from near ballarat, California. Clays and Clay Minerals 32, 147-153.
515 Pusch, R., 2006. Engineered Barriers, in: V. Popov, R. Pusch (Eds.), Disposal of hazardous waste in
516 underground mines, Wessex Institute of Technology, UK, pp. 35-40.
517 Pusch, R., Kasbohm, J., Pakovsky, J., Cechova, Z., 2007. Are all smectite clays suitable as "buffers". Physics
518 and Chemistry of the Earth 32, 116–122.
519 Sánchez-Soto, P.J., Justo, A., Pérez-Rodríguez, J.L., 1994. Griding effect on kaolinite pyrophyllite illite
520 natural mixtures and its influence on mullite formation. Journal of Materials Science 29, 1276–1283.
521 Sanz, J., Serratosa, J.M., 1984. Si-29 and Al-27 High-Resolution MAS-NMR spectra of phyllosilicates.
522 Journal of the American Chemical Society 106, 4790-4793.
523 Savage, D., Chapman, N.A., 1982. Hydrothermal behaviour of simulated waste glass- and waste-rock
524 interaction under repository conditions. Chemical Geology 36, 59-86.
525 Selvam, T., Bandarapu, B., Mabande, G.T.P., Toufar, H., Schwieger, W., 2003. Hydrothermal transformation
526 of layered sodium silicate, kanemite, into zeolite beta (BEA). Microporous and Mesoporous Materials
527 64, 41-50.
528 Smith, J.V., Blackwell, C.S., 1983. Nuclear Magnetic-Resonance of Silica Polymorphs. Nature 303, 223-225.
529 Weiss, C.A, Altaner, S.P., Kirkpatrick, R.J., 1987. High resolution ^{29}Si NMR spectroscopy of 2:1 layer
530 silicates: Correlations among chemical shift, structural distortions, and chemical variations. American
531 Mineralogist 72, 935-942.
532 Wheeler, P.A., Wang, J., Baker, J., Mathias, L.J., 2005. Synthesis and characterization of covalently
533 functionalized Laponite clay. Chemistry of Materials 17, 3012-3018.
534 Williams-Daryn, S., Thomas, R.K., Castro, M.A., Becerro A., 2002. The structures of complexes of a
535 vermiculite intercalated by cationic surfactants, a mixture of cationic surfactants, and a mixture of
536 cationic and non-ionic surfactants. Journal of Colloid and Interface Science 256, 314-324.
537

Table 1. Layered aluminosilicates used as starting materials

Silicate	Source	Chemical Formulae
Kanemite[1]	Synthetic[a]	$Na[Si_2O_4(OH)]\cdot 3H_2O$
Pyrophyllite[2]	Natural Hillsboro	$(Ca_{0.006}Na_{0.012}K_{0.018})[Si_4][Al_{1.95}Fe_{0.01}Ti_{0.005}Mg_{0.001}]O_{10}(OH)_2$
Talc[3]	Natural Lillo	$[Si_4][Mg_{2.95}Fe_{0.017}]O_{10}F_{0.19}(OH)_{1.81}$
Hectorite[4]	Natural[b] S.Bernardino	$Ca_{0.17}[Si_{3.98}Al_{0.02}][Mg_{2.65}Al_{0.02}Li_{0.33}]O_{10}(OH)_2$
Laponite®[5]	Synthetic[c]	$Na_{0.35}[Si_4][Mg_{2.73}Li_{0.2}]O_{10}(OH)_2$
Saponite[6]	Natural[b] California	$Na_{0.31}K_{0.01}Ca_{0.04}[Si_{3.6}Al_{0.4}][Mg_{2.9}Fe_{0.07}]O_{10}(OH)_2$
Vermiculite[7]	Natural Eucatex	$Na_{0.7}[Si_{3.1}Al_{0.9}][Mg_{2.48}Al_{0.08}Fe_{0.31}Ti_{0.04}Mn_{0.01}]O_{10}(OH)_2$

(a) synthesized by Alba et al. (2006); (b) Source Clays Repository of the Clay Minerals Society, *University of Missouri, Columbia, USA*; (c) Solvay Alkali GMBH

(1) Alba et al., 2006 ; (2) Sánchez Soto et al., 1994; (3) Petit et al., 2004; (4) Laporte Industries Ltd, 1990; Levitz et al., 2000; (5) Prost, 1984; Alba et al., 2001a and 2001b; (6) Ames et al., 1958; (7) Williams-Daryn et al., 2002

538

539

540

541

Table 2. ^{29}Si chemical shift, FWHM and area under the curve of the different contributions obtained from the fitting of the ^{29}Si MAS NMR spectrum of kanemite, pyrophyllite and talc.

δ (ppm)	FWHM (Hz)	%	phase
kanemite			
Starting material			
-97.3±0.1	99±1	100	Q^3(0Al)
After hydrothermal treatment in a 7.3·10^{-2} M Lu(NO$_3$)$_3$·3.6H$_2$O solution			
-91.8±0.1	97±2	11.4	$Lu_2Si_2O_7$
-100.5±0.2	134±37	0.9	$H_2Si_2O_5$
-111.5±0.1	461±3	87.7	Q^4(0Al)
pyrophyllite			
Starting material			
-95.2±0.1	111±1	100	Q^3(0Al)
After hydrothermal treatment in a 7.3·10^{-2} M Lu(NO$_3$)$_3$·3.6H$_2$O solution			
-92.1±0.1	161±11	4.3	$Lu_2Si_2O_7$
-95.0±0.1	104±1	93.9	Q^3(0Al)
-99.0±0.1	122±15	1.8	$H_2Si_2O_5$
talc			
Starting material			
-98.1±0.1	141±1	100	Q^3(0Al)
After hydrothermal treatment in a 7.3·10^{-2} M Lu(NO$_3$)$_3$·3.6H$_2$O solution			
-91.7±0.1	126±1	83.6	$Lu_2Si_2O_7$
-97.7±0.1	134±4	16.4	Q^3(0Al)

Table 3. ^{29}Si chemical shift, FWHM and area under the curve of the different contributions obtained from the fitting of the ^{29}Si MAS NMR spectrum of hectorite, Na-hectorite and Laponite®

δ (ppm)	FWHM (Hz)	%	phase
hectorite			
Starting material			
-95.0±0.1	239±2	100	Q^3(0Al)
After hydrothermal treatment in a 7.3·10^{-2} M Lu(NO$_3$)$_3$·3.6H$_2$O solution			
-79.8±0.1	629±25	16.4	X_2-Lu_2SiO_5
-86.4±0.1	687±43	27.4	enstatite
-91.4±0.1	261±15	13.3	$Lu_2Si_2O_7$
-94.6±0.1	392±16	27.1	Q^3(0Al)
-100.9±0.3	740±74	10.8	$H_2Si_2O_5$
-110.2±0.1	390±28	5.0	cristobalite
Na-hectorite			
After hydrothermal treatment in a 7.3·10^{-2} M Lu(NO$_3$)$_3$·3.6H$_2$O solution			
-84.1±0.2	481±44	7.1	enstatite
-91.6±0.1	167±6	12.7	$Lu_2Si_2O_7$
-95.3±0.1	215±28	5.8	Q^3(0Al)
-100.7±0.3	667±65	14.4	$H_2Si_2O_5$
-111.5±0.1	273±15	60.0	cristobalite
Laponite®			
Starting material			
-85.2±0.1	316±7	7.7	Q^3(0Al), $(SiO)_3SiOH$
-94.5±0.1	263±2	79.0	Q^3(0Al)
-97.3±0.1	188±5	13.3	Q^3(0Al), $(SiO)_3SiO^-$
After hydrothermal treatment in a 7.3·10^{-2} M Lu(NO$_3$)$_3$·3.6H$_2$O solution			
-90.6±0.1	258±4	27.2	δ-$Na_2Si_2O_5$
-91.7±0.1	90±1	72.8	$Lu_2Si_2O_7$

542

543

Table 4. ^{29}Si chemical shift, FWHM and area under the curve of the different contributions obtained from the fitting of the ^{29}Si MAS NMR spectrum of saponite and vermiculite eucatex

δ (ppm)	FWHM (Hz)	%	phase
saponite			
Starting material			
-85.3±0.1	55±10	0.4	Q^3(2Al)
-90.8±0.1	210±2	35.0	Q^3(1Al)
-95.8±0.1	220±1	64.6	Q^3(0Al)
After hydrothermal treatment in a $7.3\cdot10^{-2}$ M $Lu(NO_3)_3\cdot3.6H_2O$ solution			
-72.5±0.1	146±11	2.6	Q^1
-88.5±0.1	582±26	23.8	natrosilite (β-$Na_2Si_2O_5$)
-91.7±0.2	122±1	71.4	$Lu_2Si_2O_7$
-95.0±0.1	122±14	2.4	Q^3(0Al)
vermiculite eucatex			
Starting material			
-84.2±0.1	679±23	10.6	Q^3(2Al)
-88.6±0.1	590±4	40.5	Q^3(1Al)
-93.4±0.1	549±18	8.8	Q^3(0Al)
-99.6±0.2	2872±37	40.0	Q^4(0Al), $(SiO)_4SiOH$
After hydrothermal treatment in a $7.3\cdot10^{-2}$ M $Lu(NO_3)_3\cdot3.6H_2O$ solution			
-76.3±0.1	818±43	4.5	Q^1, Q^0
-88.2±0.1	828±5	37.6	natrosilite (β-$Na_2Si_2O_5$)
-91.4±0.2	212±1	57.9	$Lu_2Si_2O_7$

FIGURE CAPTIONS

Fig. 1. XRD patterns of kanemite, pyrophyllite and talc: (a) starting material, and, (b) after hydrothermal treatment at 300º C for 48 h in a $7.3 \cdot 10^{-2}$ M $Lu(NO_3)_3 \cdot 3.6H_2O$ solution. *=$Lu_2Si_2O_7$ (PDF 35-0326), T=tridymite (PDF 18-1170), H=$H_2Si_2O_5$ (PDF 74-1548), and, b=boehmite (PDF 76-1871).

Fig. 2. ^{29}Si MAS NMR (left) and ^{1}H MAS NMR (right) spectra of kanemite, pyrophyllite and talc: (a) starting material, and, (b) after hydrothermal treatment at 300º C for 48 h in a $7.3 \cdot 10^{-2}$ M $Lu(NO_3)_3 \cdot 3.6H_2O$ solution.

Fig. 3. XRD patterns of hectorite, Na-hectorite and Laponite®: (a) starting material, and, (b) after hydrothermal treatment at 300º C for 48 h in a $7.3 \cdot 10^{-2}$ M $Lu(NO_3)_3 \cdot 3.6H_2O$ solution. *=$Lu_2Si_2O_7$ (PDF 35-0326), E=enstatite (PDF 73-1937), H=$H_2Si_2O_5$ (PDF 74-1548), and, C=β-cristobalite (PDF 89-3607).

Fig. 4. XRD patterns of saponite and vermiculite Eucatex: (a) starting material, and, (b) after hydrothermal treatment at 300º C for 48 h in a $7.3 \cdot 10^{-2}$ M $Lu(NO_3)_3 \cdot 3.6H_2O$ solution. *=$Lu_2Si_2O_7$ (PDF 35-0326), M=$H(Mg_2(SiO_4))_8$ (PDF 87-2051), O=$Mg_{10}(Si_3O_{14})(OH)_4$ (PDF 81-544), k=kaolinite (PDF 78-1996), and, n=natrosilite (PDF 23-0529).

Fig. 5. ^{29}Si MAS NMR (left) and ^{1}H MAS NMR (right) spectra of hectorite, Na-hectorite and Laponite®: (a) starting material, and, (b) after hydrothermal treatment at 300º C for 48 h in a $7.3 \cdot 10^{-2}$ M $Lu(NO_3)_3 \cdot 3.6H_2O$ solution.

Fig. 6. ^{29}Si MAS NMR (left), ^{1}H MAS NMR (middle) and ^{27}Al MAS NMR (right) spectra of saponite and vermiculite Eucatex: (a) starting material, and, (b) after hydrothermal treatment at 300º C for 48 h in a $7.3 \cdot 10^{-2}$ M $Lu(NO_3)_3 \cdot 3.6H_2O$ solution.

568

Fig. 1

569

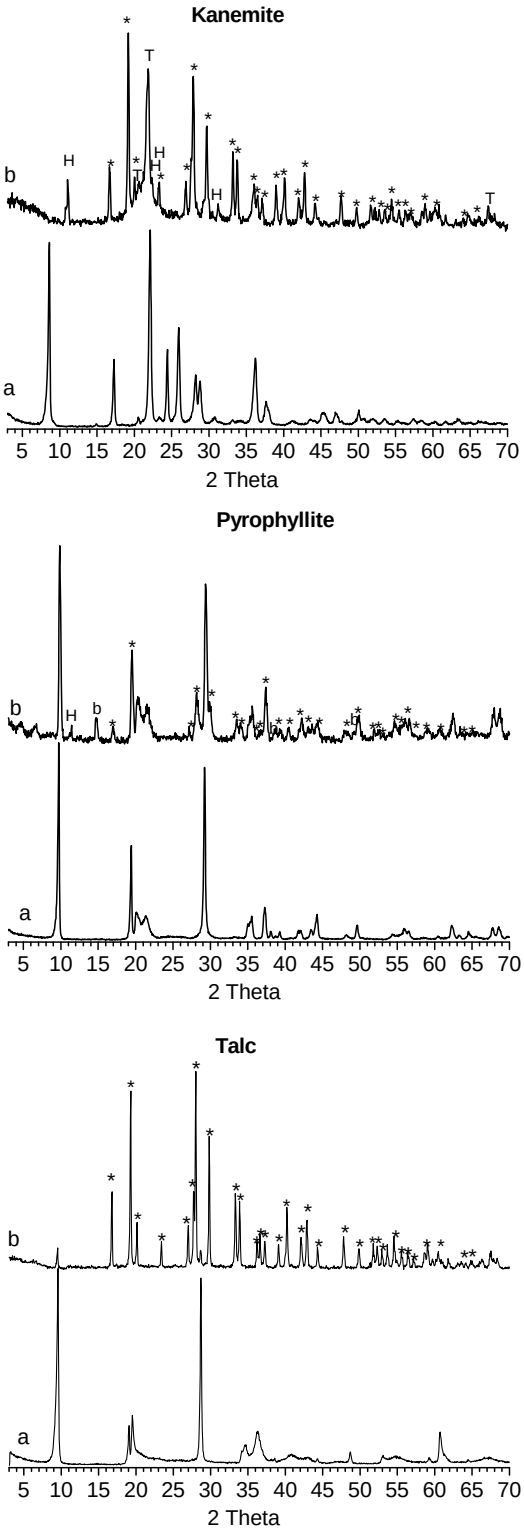
Kanemite
b
a
H
T
2 Theta
Pyrophyllite
b
a
H
b
2 Theta
Talc
b
a
2 Theta
5 10 15 20 25 30 35 40 45 50 55 60 65 70

570

Fig. 2

571

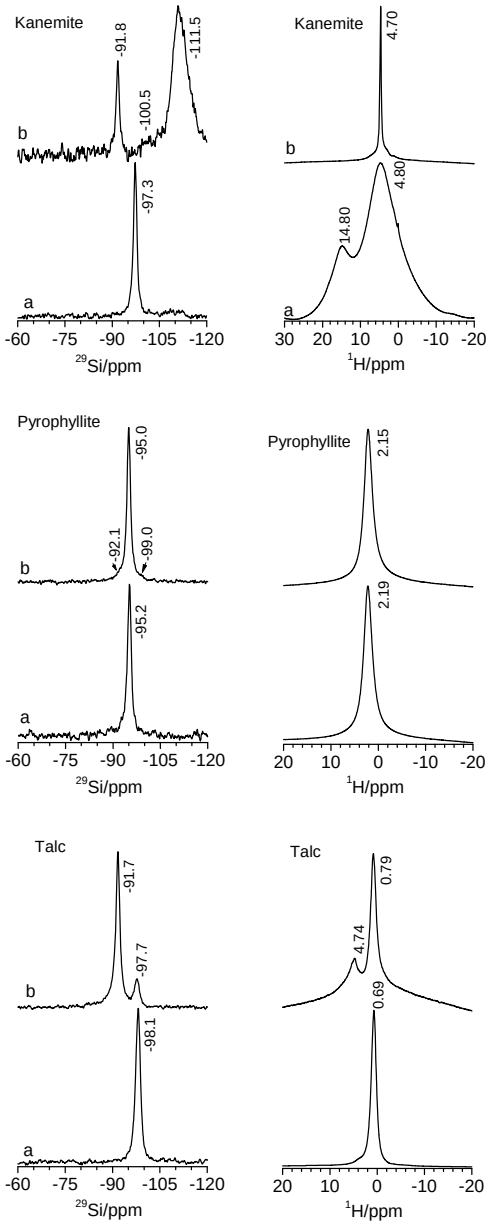
Kanemite
-91.8
-111.5
-100.5
b
-97.3
a
-60 -75 -90 -105 -120
29Si/ppm
Kanemite
4.70
b
4.80
14.80
a
30 20 10 0 -10 -20
1H/ppm
Pyrophyllite
-95.0
-92.1
-99.0
b
-95.2
a
-60 -75 -90 -105 -120
29Si/ppm
Pyrophyllite
2.15
2.19
20 10 0 -10 -20
1H/ppm
Talc
-91.7
-97.7
b
-98.1
a
-60 -75 -90 -105 -120
29Si/ppm
Talc
0.79
4.74
0.69
20 10 0 -10 -20
1H/ppm

572

Fig. 3

573

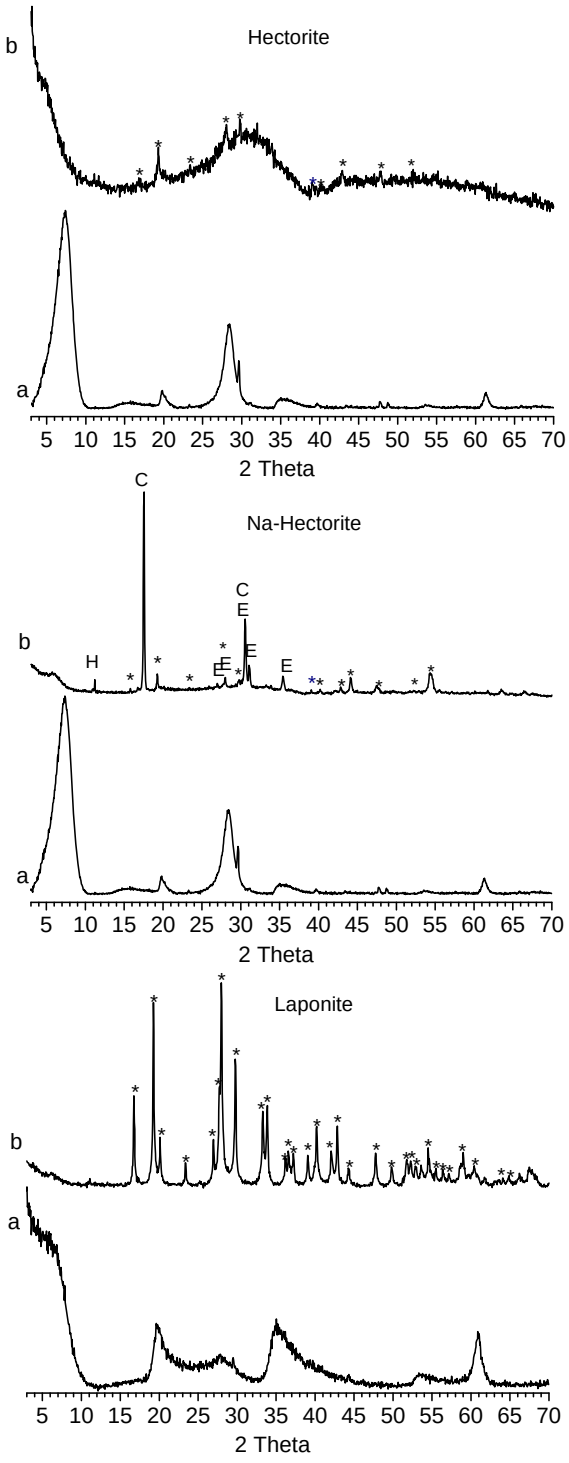
Hectorite
b
a
5 10 15 20 25 30 35 40 45 50 55 60 65 70
2 Theta
Na-Hectorite
C
C
E
H
E
E
E
E
b
a
5 10 15 20 25 30 35 40 45 50 55 60 65 70
2 Theta
Laponite
b
a
5 10 15 20 25 30 35 40 45 50 55 60 65 70
2 Theta

574

575

576

Fig. 4

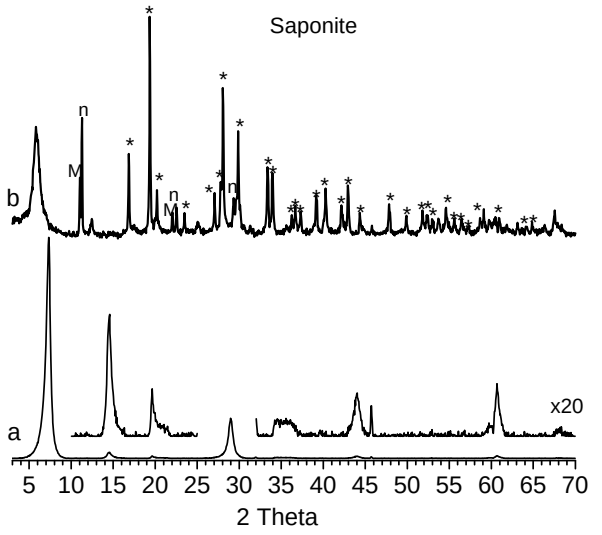

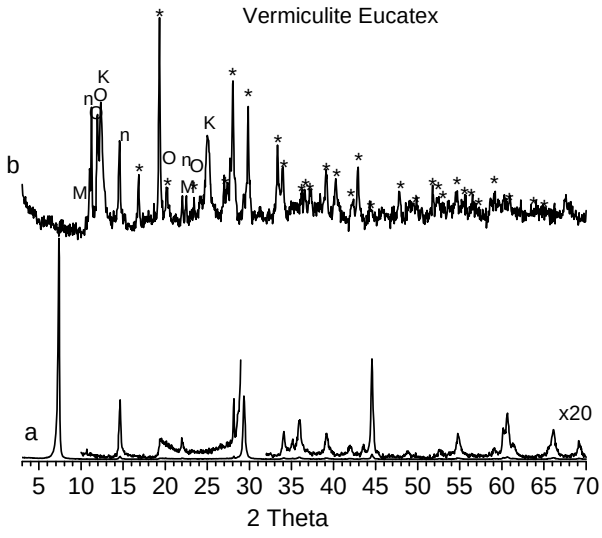

577

578

579

Fig. 5

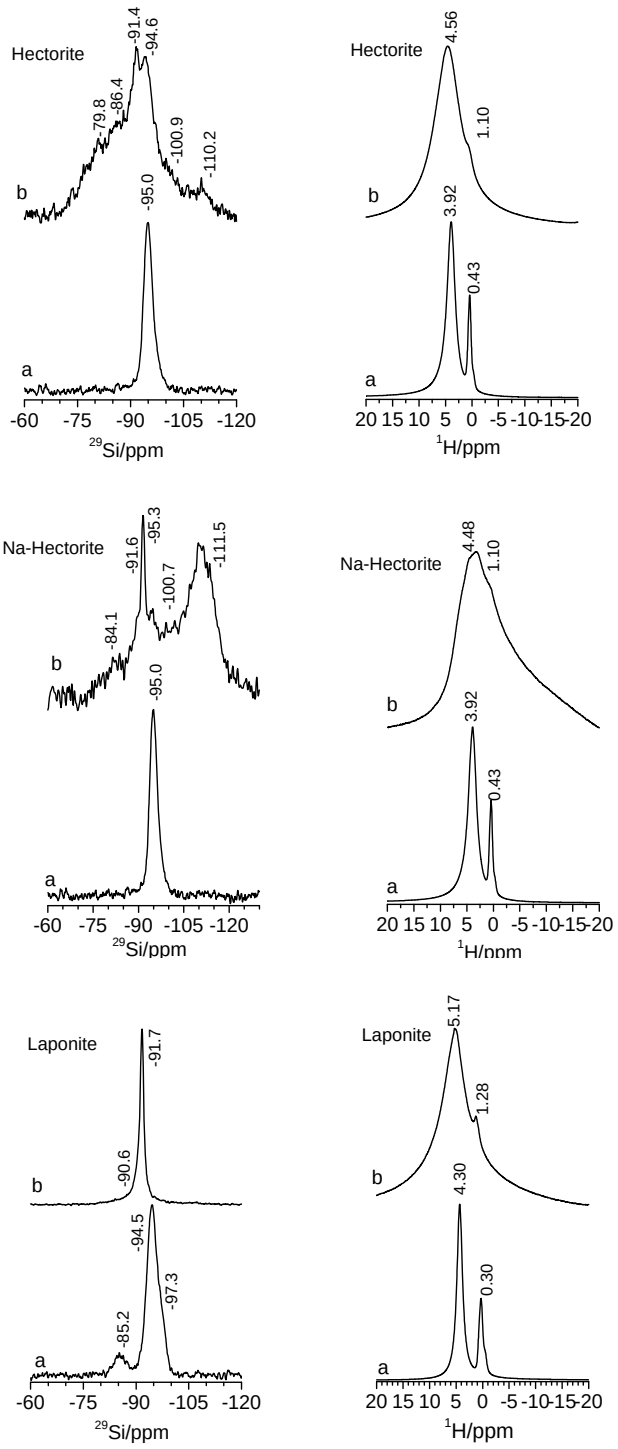

580

581 *Fig. 6*

582

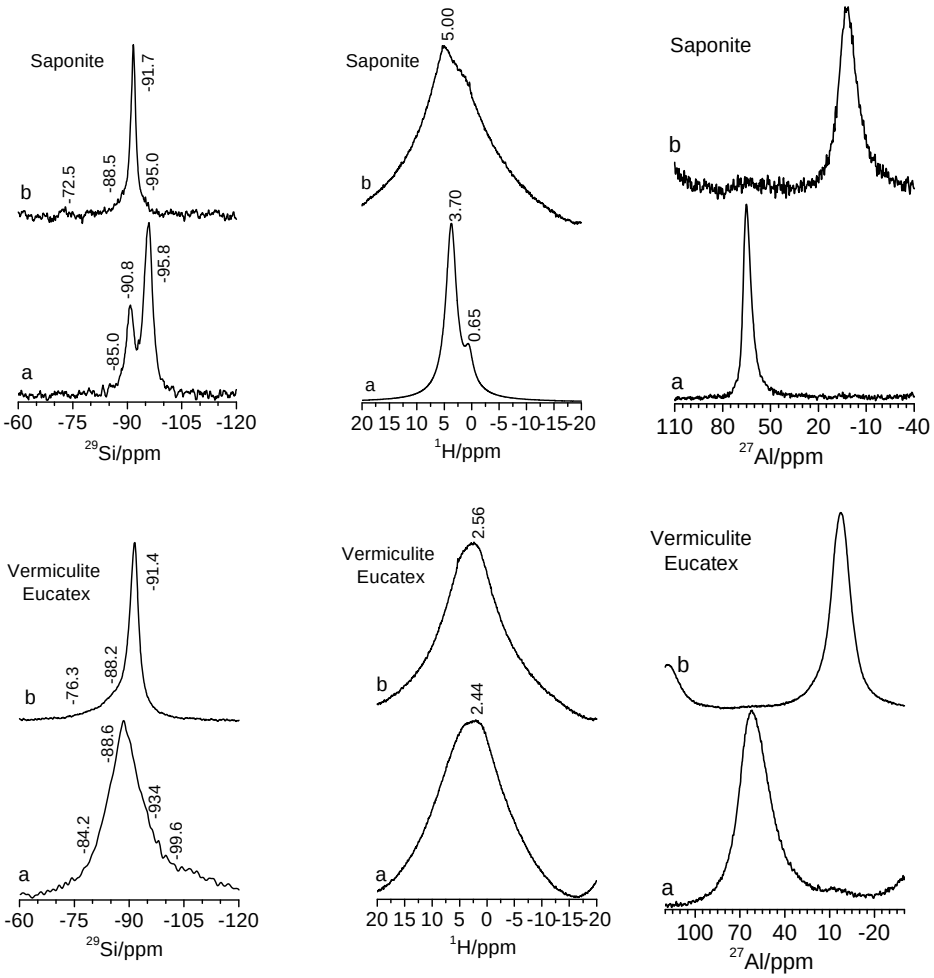

583